AIAA JOURNAL
Vol. 47, No. 3, March 2009

Implicit Large-Eddy Simulation of Swept-Wing Flow Using High-Resolution Methods

M. Hahn* and D. Drikakis†
Cranfield University, Cranfield, England MK43 0EB, United Kingdom

DOI: 10.2514/1.37806

A numerical investigation of a fully three-dimensional swept-wing geometry featuring separation from a curved leading edge is presented. The implicit large-eddy-simulation strategy based on a third-order high-resolution method for discretizing the advective fluxes and a second-order Runge–Kutta time-stepping scheme with an extended stability region have been employed. No attempt to incorporate a wall model has been made. Instead, the boundary layer is fully resolved over the majority of the wing. Qualitative and quantitative comparisons with experimental oil-film visualizations and three-dimensional laser Doppler anemometry measurements show very good agreement between the experiment and the numerically predicted flow structures, as well as velocity and stress profiles near the wing. Furthermore, data from a hybrid Reynolds-averaged Navier–Stokes and large-eddy simulation have been included for comparison.

Nomenclature

$\mathbf{E}, \mathbf{F}, \mathbf{G}$	=	convective fluxes
e	=	total energy per unit volume
$\mathbf{I}$	=	identity tensor
p	=	pressure
$\mathbf{q}$	=	heat flux
R	=	gas constant
$\mathbf{R}, \mathbf{S}, \mathbf{L}$	=	viscous fluxes
T	=	temperature
$\mathbf{U}$	=	conservative variables
$\mathbf{u}$	=	velocity vector
μ	=	dynamic viscosity
ρ	=	density

Subscripts

i	=	control volume index
$i \pm 1/2$	=	intercell position

Superscripts

n	=	current time step
1, 2	=	intermediate time steps

I. Introduction

ONE of the greatest challenges for current large-eddy simulations is the application to flow problems of practical engineering interest. In the context of aeronautical applications, curved three-dimensional geometries such as swept and delta wings are among the most difficult scenarios encountered, because they are prone to transition and separation. Swept and delta wings can be found in all modern aircraft and unmanned air vehicles traveling at subsonic, transonic, or supersonic speeds. However, it is not only cruise conditions that are of aerodynamic interest. Most of these vehicles also fly a considerable amount of time at subsonic speeds and moderate-to-high angles of attack (e.g., takeoff and landing or air combat). In fact, the nonlinear effects associated with separation at these flow conditions are more interesting from the modeler's point of view and much more difficult to simulate accurately [1]. Computational challenges include the prediction of transition leading to turbulence, unsteady separation, optimum balance of numerical dissipation and dispersion, and adequate grid generation for achieving accurate and efficient solutions.

Computational studies of separated swept-wing flows have traditionally been focused on sharp-edged delta geometries, because the detachment process is greatly simplified. Various combinations of slender and nonslender delta wings at different angles of attack between 5 and 30 deg have been investigated for Reynolds numbers ranging from the order of 10^4 to 10^6 using Reynolds-averaged numerical simulations (RANS), large-eddy simulations (LES), and hybrid simulations [2–6]. Although transition and separation from curved wing surfaces is a prime concern, all previous studies have been limited to quasi-infinite aerofoil sections (e.g., the European LESFOIL project on large-eddy simulations around an Aerospatiale A-aerofoil near stall conditions at an angle of incidence of 13.3 deg [7]. Past studies have shown that near-wall resolution is of paramount importance for accurately predicting this type of flow. This impression has been confirmed by implicit large-eddy simulation (ILES) simulations [8] and results obtained from a local 2-D/3-D-coupling LES approach [9,10]. These investigations have been conducted at high Reynolds numbers on the order of 10^6. To obtain a fully resolved solution of a similar flowfield, however, the Reynolds number has to be decreased by 1 order of magnitude because of the current hardware limitations (e.g., for direct numerical simulations for a NACA 0012 aerofoil, see [11]).

Although a great deal of attention has been paid to complex separated-flow structures for wings at relatively high angles of incidence, a theoretical or computational model for predicting the flow behavior with any degree of certainty has not emerged yet. In fact, no attempt at combining realistic conditions for the flow detachment with a leading-edge sweep has been made to date. This investigation is thus concerned with a fully three-dimensional swept-wing geometry featuring separation from a smoothly curved leading edge. Here, the resulting flowfield is highly complex, nonlinear, and characterized by transition zones, leading-edge (and possible trailing-edge) separation, vortical flow, turbulence, secondary separated zones, and reattachment.

The ILES technique employed here is based on high-resolution methods [12,13]. The ILES approach is currently used to simulate a range of complex wall-bounded flows, such as open cavities [13],

Presented as Paper 669 at the 46th AIAA Aerospace Sciences Meeting and Exhibit, Reno, NV, 7–10 January 2008; received 31 March 2008; revision received 24 October 2008; accepted for publication 5 November 2008.

*Research Officer, Fluid Mechanics and Computational Science Group, Department of Aerospace Sciences, School of Engineering.

†Professor, Head of Fluid Mechanics and Computational Science Group, Department of Aerospace Sciences, School of Engineering.

plane channels [14], backward-facing steps [15], or submarine hydrodynamics [16]. In addition, rigorous analytical justifications of the applicability of this class of numerical schemes to flows dominated by turbulence has been attempted [12,17,18]. A comprehensive discussion of ILES has also been published in the form of a book [19]. The success of high-resolution methods to compute both low- and high-speed turbulent flows seems to depend on a delicate balance of truncation errors due to wave-speed-dependent terms (chiefly responsible for numerical dissipation) and the hyperbolic part of the convective flux. It is the essence of this balance that regularizes the flow and allows the phenomena to be captured physically realistically, even if they are not fully resolved on the computational mesh.

II. Numerical Framework

A. Governing Equations

The physics of (Newtonian) fluid flow is governed by the Navier–Stokes equations. They are solved by considering the coupled generalized conservation laws (namely, the continuity, momentum, and energy equations):

$$\frac{\partial \rho}{\partial t} + \nabla \cdot (\rho \mathbf{u}) = 0 \tag{1}$$

$$\frac{\partial \rho \mathbf{u}}{\partial t} + \nabla \cdot (\rho \mathbf{u}\mathbf{u}) = -\nabla \cdot \mathbf{P} \tag{2}$$

$$\frac{\partial e}{\partial t} + \nabla \cdot (e\mathbf{u}) = -\nabla \cdot (\mathbf{P} \cdot \mathbf{u}) - \nabla \cdot \mathbf{q} \tag{3}$$

where $\mathbf{u}$, ρ, e, and $\mathbf{q}$ stand for the velocity components, density, total energy per unit volume, and heat flux, respectively. The tensor $\mathbf{P}$ for a Newtonian fluid is defined by

$$\mathbf{P} = p(\rho, T)\mathbf{I} + \tfrac{2}{3}\mu(\nabla \cdot \mathbf{u})\mathbf{I} - \mu[(\nabla \mathbf{u}) + (\nabla \mathbf{u})^T] \tag{4}$$

where $p(\rho, T)$ is the scalar pressure, $\mathbf{I}$ is the identity tensor, T is the temperature, and μ is the dynamic viscosity coefficient. The preceding system is completed by an equation of state. For a perfect gas, the equation of state is given by $p = \rho RT$, where R is the gas constant.

To facilitate the development of numerical methods, Eqs. (1–3) are written in Cartesian matrix form [12] as

$$\frac{\partial \mathbf{U}}{\partial t} + \frac{\partial \mathbf{E}}{\partial x} + \frac{\partial \mathbf{F}}{\partial y} + \frac{\partial \mathbf{G}}{\partial z} = \frac{\partial \mathbf{R}}{\partial x} + \frac{\partial \mathbf{S}}{\partial y} + \frac{\partial \mathbf{L}}{\partial z} \tag{5}$$

where $\mathbf{U}$ is the array of the conservative variables; $\mathbf{E}$, $\mathbf{F}$, and $\mathbf{G}$ are the inviscid flux vectors and $\mathbf{R}$, $\mathbf{S}$, and $\mathbf{L}$ are the viscous flux vectors associated with the Cartesian x, y, and z directions, respectively:

$$\mathbf{U} = [\rho, \rho u, \rho v, \rho w, e]^T$$

$$\mathbf{E} = [\rho u, \rho u^2 + p, \rho vu, \rho wu, (e + p)u]^T$$

$$\mathbf{F} = [\rho v, \rho uv, \rho v^2 + p, \rho wv, (e + p)v]^T$$

$$\mathbf{G} = [\rho w, \rho uw, \rho vw, \rho w^2 + p, (e + p)w]^T$$

$$\mathbf{R} = [0, \tau_{xx}, \tau_{xy}, \tau_{xz}, u\tau_{xx} + v\tau_{xy} + w\tau_{xz} - \dot{q}_x]^T$$

$$\mathbf{S} = [0, \tau_{yx}, \tau_{yy}, \tau_{yz}, u\tau_{yx} + v\tau_{yy} + w\tau_{yz} - \dot{q}_y]^T$$

$$\mathbf{L} = [0, \tau_{zx}, \tau_{zy}, \tau_{zz}, u\tau_{zx} + v\tau_{zy} + w\tau_{zz} - \dot{q}_z]^T$$

To allow for body-fitted grids, Eq. (5) has to be transformed to generalized curvilinear coordinates given by $\xi = \xi(x, y, z, t)$, $\eta = \eta(x, y, z, t)$, $\zeta = \zeta(x, y, z, t)$, and $\tau = t$. Subsequently, the viscous terms are discretized using a central-difference scheme and the advective flux derivatives are solved by applying a characteristics-based high-resolution method.

B. Characteristics-Based High-Resolution Scheme

For the sake of simplicity, only the Cartesian flux derivative $\partial \mathbf{E}/\partial x$ is considered here. The discretization at the center of the control volume (i) using the values of the intercell fluxes yields

$$\frac{\partial \mathbf{E}}{\partial x} = \frac{\mathbf{E}_{i+1/2} - \mathbf{E}_{i-1/2}}{\Delta x} \tag{6}$$

The intercell flux functions $\mathbf{E}_{i+1/2}$ and $\mathbf{E}_{i-1/2}$ are calculated according to a characteristics-based scheme [20–22] that satisfies the following criteria for high-resolution methods [23]:

1) Provide at least second-order accuracy in smooth areas of the flow.

2) Produce numerical solutions (relatively) free from spurious oscillations.

3) In the case of discontinuities, the number of grid points in the transition zone containing the shock wave is smaller than that of first-order monotone methods.

The characteristics-based scheme is a Godunov-type method that defines the conservative variables along the characteristics as functions of their characteristic values. A third-order-accurate MUSCL-type reconstruction [24] has been used here to compute the left and right states of the conservative variables $\mathbf{U}$ at the cell interface $(i + 1/2)$ according to

$$\begin{aligned}
\bar{\mathbf{U}}_{L,i+1/2} &= \mathbf{U}_i + \frac{1}{4}\Bigg[(1-k)\phi(r_L)(\mathbf{U}_i - \mathbf{U}_{i-1}) \\
&\quad + (1+k)\phi\left(\frac{1}{r_L}\right)(\mathbf{U}_{i+1} - \mathbf{U}_i)\Bigg] \\
\bar{\mathbf{U}}_{R,i+1/2} &= \mathbf{U}_{i+1} - \frac{1}{4}\Bigg[(1-k)\phi(r_R)(\mathbf{U}_{i+2} - \mathbf{U}_{i+1}) \\
&\quad + (1+k)\phi\left(\frac{1}{r_R}\right)(\mathbf{U}_{i+1} - \mathbf{U}_i)\Bigg]
\end{aligned} \tag{7}$$

where k is a free parameter in the interval $[-1, 1]$ and ϕ is a limiter function based on the slopes of the conserved variables. For $k = -1$ or 0, the MUSCL extrapolation [25] is essentially a full upwind scheme or a central-difference scheme, respectively, and third-order accuracy can be obtained for $k = 1/3$ if the limiter is not entirely symmetric. The left and right ratios of the slopes are defined as

$$r_L = \frac{\mathbf{U}_{i+1} - \mathbf{U}_i}{\mathbf{U}_i - \mathbf{U}_{i-1}}, \qquad r_R = \frac{\mathbf{U}_{i+1} - \mathbf{U}_i}{\mathbf{U}_{i+2} - \mathbf{U}_{i+1}}, \tag{8}$$

and the limiter function is calculated as

$$\phi = \begin{cases} 0 & \text{if } r \le 0 \\ 1 - \left(1 + \frac{2Nr}{1+r^2}\right)\left(1 - \frac{2r}{1+r^2}\right)^N & \text{if } r > 0 \end{cases} \tag{9}$$

This formulation of the third-order limiter includes a steepening parameter N that improves the resolution of discontinuities. For general use, N is set equal to 2.

Along each characteristic (denoted by $l = 0, 1, 2$), the variables $\mathbf{U}_l$ are then given by

$$\mathbf{U}_{l,i+1/2} = (0.5 + \psi_l)\bar{\mathbf{U}}_{L,i+1/2} + (0.5 - \psi_l)\bar{\mathbf{U}}_{R,i+1/2} \tag{10}$$

where the function ψ_l is defined as

$$\psi_l = 0.5\frac{\lambda_{L,l} + \lambda_{R,l}}{|\lambda_{L,l}| + |\lambda_{R,l}| + \epsilon} \tag{11}$$

The parameter ϵ averts division by zero and $\lambda_{L,l}$ and $\lambda_{R,l}$ are the left and right eigenvalues at the cell face, respectively. Using the Godunov-type upwinding scheme from Eq. (10), three sets of characteristic variables are calculated:

$$\mathbf{U}_{0,i+1/2} = \begin{pmatrix} \rho_0 \\ (\rho u)_0 \\ (\rho v)_0 \\ (\rho w)_0 \\ e_0 \end{pmatrix}, \qquad \mathbf{U}_{1,i+1/2} = \begin{pmatrix} \rho_1 \\ (\rho u)_1 \\ (\rho v)_1 \\ (\rho w)_1 \\ e_1 \end{pmatrix}$$
$$\mathbf{U}_{2,i+1/2} = \begin{pmatrix} \rho_2 \\ (\rho u)_2 \\ (\rho v)_2 \\ (\rho w)_2 \\ e_2 \end{pmatrix} \tag{12}$$

With the characteristic variables $\mathbf{U}_{l,i+1/2}$ being known, the characteristics-based variables $\hat{\mathbf{U}}_{i+1/2}$ are computed according to

$$\hat{\mathbf{U}}_{i+1/2} = \begin{pmatrix} \hat{\rho} \\ (\widehat{\rho u}) \\ (\widehat{\rho v}) \\ (\widehat{\rho w}) \\ \hat{e} \end{pmatrix} = \begin{pmatrix} \rho_0 + r_1 + r_2 \\ (\rho u)_0 + (u+s)r_1 + (u-s)r_2 \\ (\rho v)_0 + v r_1 + v r_2 \\ (\rho w)_0 + w r_1 + w r_2 \\ e_0 + (H + s\lambda_0)r_1 + (H - s\lambda_0)r_2 \end{pmatrix} \tag{13}$$

where H is the total enthalpy:

$$H = \frac{s^2}{\gamma - 1} + 0.5q^2 \tag{14}$$

Here, q is given by $q^2 = u^2 + v^2 + w^2$ and r_1, r_2 are functions of the characteristic variables; the flow velocities u, v, and w; and the speed of sound s. Finally, the advective flux $\mathbf{E}_{i+1/2}$ for the characteristics-based scheme is calculated using the variables $\hat{\mathbf{U}}_{i+1/2}$, yielding

$$\mathbf{E}^{CB}_{i+1/2} = \mathbf{E}(\hat{\mathbf{U}}_{i+1/2}) \tag{15}$$

C. Time Integration

For integrating the system of governing equations in time, an explicit Runge–Kutta time-stepping method was chosen. In highly unsteady flows such as swept-wing flows, explicit time marching is preferred to an implicit treatment because of the need to temporally resolve the rapidly fluctuating components.

The Runge–Kutta method employed here is second-order-accurate in time [26] and consists of the following stages:

$$\frac{\mathbf{U}^1 - \mathbf{U}^n}{h} = \frac{1}{2} f(\mathbf{U}^n, t^n), \qquad \frac{\mathbf{U}^2 - \mathbf{U}^1}{h} = \frac{1}{2} f(\mathbf{U}^1, t^{n+1/3})$$
$$\frac{\mathbf{U}^{n+1} - \frac{2}{3}\mathbf{U}^2 - \frac{1}{3}\mathbf{U}^n}{h} = \frac{1}{3}[f(\mathbf{U}^2, t^{n+2/3})] \tag{16}$$

where $h = \Delta t$ is the size and n is the number of the time step, respectively. Additionally, this method belongs to the group of strong stability-preserving schemes [26] and features numerical stability for Courant–Friedrichs–Lewy (CFL) numbers up to 2. In the present simulation, however, a more conservative value of CFL = 1.4 has been chosen.

III. Computational Grid

The twisted swept-wing geometry considered in this investigation was specifically designed in the framework of the MSTTAR (Modelling and Simulation of Transition and Turbulence in Aeronautics) program for the validation of CFD codes. In the associated experimental campaign, conducted at Manchester University,[‡] a wind-tunnel model featuring a leading-edge sweep angle of 40 deg, a trailing-edge sweep angle of 10.56 deg, and an effective angle of attack of 1.23 deg was used. The root chord length was approximately 0.3 m, and the span was 0.65 m with a taper ratio of 0.3.

[‡]Private communication with S. Zhang and J. T. Turner, Manchester University, 2007.

To capture the leading-edge curvature as accurately as possible and to achieve an efficient distribution of grid cells around the wing, a C-O-type topology has been chosen. After preliminary computations on a very coarse grid consisting of approximately 3.5 million cells and spanning a large computational domain, the clustering near the wing surface has been modified and the extent of the domain has been significantly reduced. The results presented here have been obtained on a grid comprising a total of 12.5 million cells in a computational domain of 6, 6.14, and 5c (c is the root chord length) in the x, y, and z directions, respectively. During the mesh generation using the commercial software GRIDGEN, the structured grid has been split into eight blocks of approximately $95 \times 130 \times 127$ cells in the streamwise, spanwise, and normal directions (see Fig. 1a), and the grid quality has been improved by applying the in-built elliptic smoothing algorithm.

The characteristic parameters specifying the grid clustering near and on the surface of the swept wing, as illustrated in Figs. 1b and 1c, are detailed in Table 1; for a definition of the corresponding edges, see Fig. 2. Here, the geometric growth rate does not exceed 1.05 in any direction, and the resulting $z+$ values range from 1 in areas of separated flow, to over 3 in reattachment regions, to 5 at the leading edge. The nondimensional grid distance [27] $z+$ is calculated as

$$z+ = \frac{u_\tau \Delta n}{\nu} \tag{17}$$

where

$$u_\tau = \sqrt{\frac{\tau_w}{\rho}}$$

is the friction velocity, and τ_w is the wall shear stress given by

$$\tau_w = \rho \nu \left. \frac{d\langle u_\parallel \rangle}{dn} \right|_{\text{wall}} \tag{18}$$

where Δn is the wall-normal distance of the cell center, $\langle u_\parallel \rangle$ is the averaged velocity component parallel to the wall, and its gradient is calculated with respect to the wall-normal direction.

Although this indicates a wall-resolved situation over the majority of the wing, the flowfield is still far from being fully resolved on the computational mesh, even in the areas near the wing tips, where the clustering is particularly fine. To quantify the degree of under-resolution, the Kolmogorov length scale has been approximated for the current flow conditions to be $5 \times 10^{-5} c$, based on the relations given for isotropic turbulence [27] and a very conservative estimate for the integral length scale of 0.5c. A detailed assessment of the numerical accuracy of the high-resolution method employed here [28] shows that it requires about 10 grid cells for the representation of the highest wave numbers to accurately describe decaying homogeneous turbulence in a statistical sense. With the data from Table 1, this roughly yields a 5-million-fold under-resolved flowfield near the tips of the swept wing. Furthermore, the shear layer emanating from the leading edge of the wing, discussed in Sec. IV.A, also cannot be adequately resolved on the given computational mesh, and there are regions with only 6 cells across the shear layer. This affects its representation in the simulation and the subsequent flow development examined in the following sections.

IV. Results

The simulation for the MSTTAR wing at a total angle of attack of 9 deg has been carried out at a Reynolds number of approximately 210,000, based on freestream velocity and root chord length, and a near incompressible Mach number of 0.3. These conditions have been chosen according to the experiments conducted at Manchester University (see footnote [‡]). The experimental data presented here include surface oil-film flow visualizations and both velocity and turbulence energy profiles inside the boundary layer, as obtained by laser Doppler anemometry (LDA).

Furthermore, comparisons with results from a hybrid RANS/LES simulation [29] of the identical case will be drawn. In the

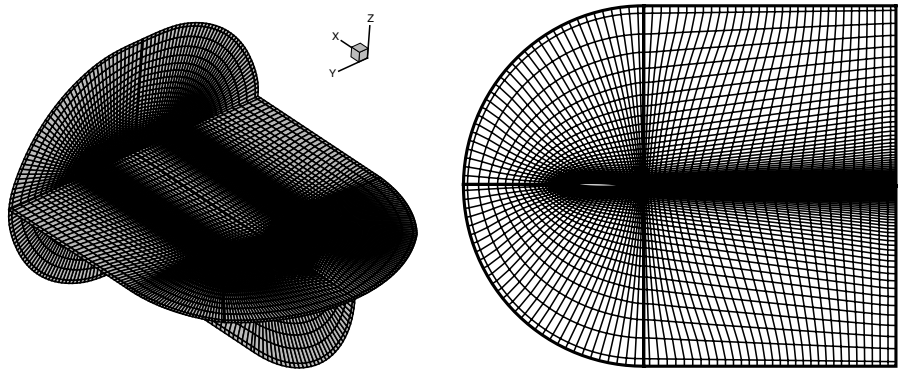

a) 3-D view of the computational grid

b) 2-D slice at the root of the wing

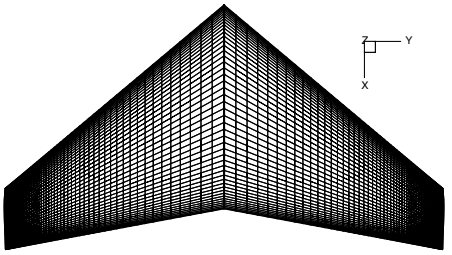

c) Surface grid (every second point)

Fig. 1 C-O-type grid topology comprising 12.5 million cells in a computational domain extending 6, 6.14, and 5*c* in the *x*, *y*, and *z* directions, respectively, (every third grid point is shown here unless stated otherwise).

incompressible hybrid RANS/LES approach, a classical second-order-accurate central-difference scheme has been employed for the spatial discretization, and the subgrid stresses are calculated using a dynamic Smagorinsky model. The time discretization is based on a second-order fractional-step algorithm and the fluxes are integrated using an Adams–Bashfort scheme. To overcome the stringent grid requirements close to the wing surfacem a two-layer zonal approach has been chosen for approximating the near-wall region [30,31]. The hybrid RANS/LES strategy applied to the MSTTAR swept wing presented here incorporates coupling of the RANS-type unsteady-boundary-layer equations, solved in the near-wall region using a simplified framework by neglecting the advection and pressure terms, with the classical LES approach used in the remainder of the computational domain [29,32].

All results presented in the following sections have been nondimensionalized with the freestream velocity and the root chord length. To obtain converged statistical averages, it was sufficient to consider a time window equivalent to two flow-through cycles. Although the length of the time window is not formally correlated to the extent of the computational domain, this information is presented here to put it into perspective. The total runtime, including the flow development from an initial condition based on the coarse grid solution, was 60,000 CPU hours on an IBM eServer POWER5 1.5 Ghz processors.

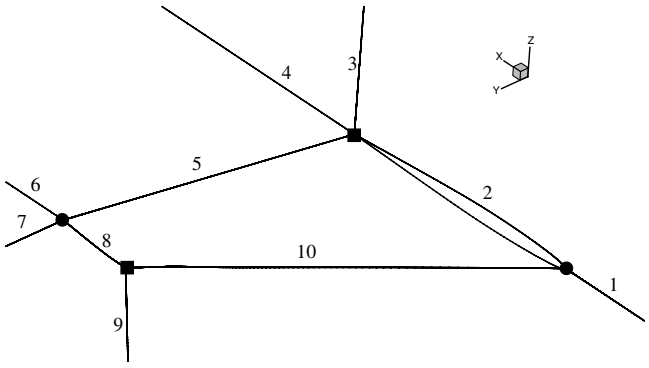

Fig. 2 Edges employed for the grid clustering in the mirror-symmetric computational domain as specified in Table 1. All other edges feature an equidistant distribution of nodes.

A. Flow Topology

The general topology of the flow around the swept-wing geometry is illustrated in Fig. 3 by instantaneous streamlines, slices of isovorticity contours, and pressure coefficient distribution on the suction side of the wing. Similar to sharp-edged delta wings, the

Table 1 Characteristic parameters specifying the point clustering in the immediate vicinity of the three-dimensional wing surface. A definition of the corresponding edges can be found in Fig. 2, in which the beginning and end of the edges are marked by ■ and ●, respectively

Edge	Nodes	Distribution	Δ_{beg}/c	Δ_{end}/c
1	128	Geometric progression	——	5.0×10^{-4}
2	96	GENERAL	3.3×10^{-3}	3.3×10^{-3}
3	128	Geometric progression	5.0×10^{-4}	——
4	96	Monotonic rational quadratic spline	3.3×10^{-3}	3.8×10^{-2}
5	131	General	3.0×10^{-2}	1.0×10^{-3}
6	96	Monotonic rational quadratic spline	——	1.0×10^{-3}
7	128	Geometric progression	——	1.0×10^{-3}
8	96	General	1.0×10^{-3}	1.0×10^{-3}
9	128	Geometric progression	1.0×10^{-3}	——
10	131	General	1.0×10^{-3}	3.0×10^{-2}

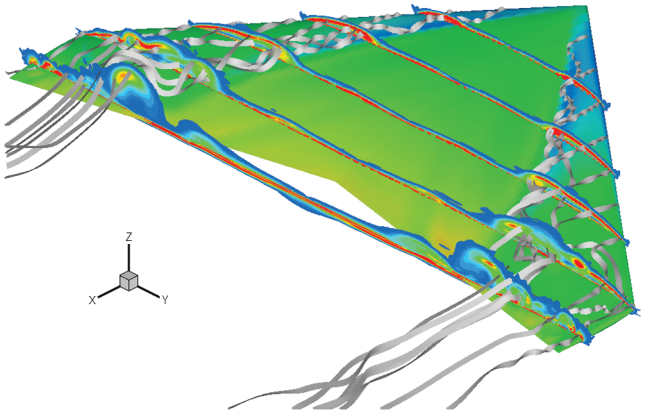

Fig. 3 Instantaneous streamlines, slices of isovorticity contours, and pressure coefficient distribution on the suction side of the wing.

shear layer emanating from the leading edges rolls up into a distinctive leading-edge vortex (LEV) system that grows and becomes less stable as it progresses toward the trailing edge. After about 50% of the root chord, the LEVs start bending inboard and lift off the wing surface at an increasing rate. The main vortex cores are associated with the large regions of vorticity still visible near the trailing edge. However, as they are less coherent than near the leading edge and are influenced by the fully turbulent flow near the wing tips, they exhibit strong fluctuations and are not symmetrical anymore.

A comparison between time-averaged streamlines just above the wing surface obtained by the present simulation and the experimental oil-film visualization is shown in Fig. 4. The computational results in the right-hand half of the picture also include contours of the pressure coefficient on the suction side of the wing. Several common flow features, marked by dashed lines for the experimental data, can be observed in both parts of the picture. The reattachment of the leading-edge vortex is well defined in the computations inboard of approximately 30%s, but starts to diffuse and bend toward the trailing edge as the LEV becomes less coherent. Close to the wing root, the reattachment line exhibits a similar angle for both the experiment and the simulation. However, the deviation from a straight line on the right-hand side appears to begin before the deviation observed on the left-hand side. This indicates premature nonlinear spreading of the leading-edge vortex in the simulation and leads to a larger extent near the trailing edge. Moreover, the two saddles SA1 and SA2 identify the existence of a secondary vortical region induced by the primary vortex along the leading edge, which can also be observed in the experiment, albeit this behavior is less clear in the oil-film visualization. The secondary vortical zone does collapse, however, as the influence of the main vortex decreases toward the wing tip due to the breakdown of its core. Although the streamlines are not following the core of the leading-edge vortex, breakdown is clearly indicated by the stagnation point between 50 and 60%s. It should be noted that a stagnation point is not visible in the experiment, and thus the LEV might still be intact. Yet, another

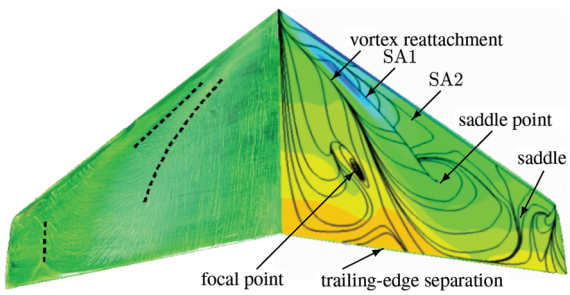

Fig. 4 Time-averaged streamlines just above the wing surface and contours of pressure coefficient as predicted by the present simulation (right). Surface oil-film visualization from experiment on the suction side of the wing (left).

feature of the flow is apparent closer to the wing tip. In the fully turbulent region, the effect of the LEV drives the fluid toward the wing tip, where it meets the opposing outer flow between 80 and 90%s. Thus, the characteristic saddle (SA) observed in both experiment and simulation is formed.

In general, the numerically predicted streamline pattern is found to be in good agreement with the oil-film visualization from the experiments. However, the skin-friction lines inboard of the main vortex in the experimental picture are aligned in the freestream direction, suggesting a simple dead-air region, whereas the simulation predicts a weakly detached region of fluid revolving around a focal point. Furthermore, an incipiently separated zone near the trailing edge, not existent in the experiment, can be seen in the computation. This observation is not exclusive to the present results, but has also been reported for hybrid RANS/LES simulations of the same case [33].

To illustrate the structural composition of the leading-edge vortex as it progresses across the wing, color contours of the Q criterion [34] are shown in Fig. 5. The two-dimensional slices are taken at constant spanwise positions ranging from 30 to 90%s. A strong and coherent LEV close to the wing surface can be identified near the root at 30%s, and the clearance between the vortex core and the wing surface increases further outboard (i.e., at 50%s).

Additionally, the secondary vortical region is clearly visible for the first two locations. At 70% half-span, the LEV has become unstable and structural integrity can no longer be observed. Closer to the wing tip (Fig. 5d), the shear layer emanating from the leading edge undergoes a roll-up similar to a Kelvin–Helmholtz mechanism, and the resulting flow is akin to vortex shedding.

Figure 6 shows the evolution of the clearance between the center position of the leading-edge vortex and the wing surface across the span. Here, data from the experiment, the present ILES, and the results from the hybrid RANS/LES computation are included for sections inboard of vortex breakdown. Both simulations and the experiment exhibit a similar vortex growth as it develops toward the wing tip; however, the numerically predicted clearance is slightly higher than in the experiment, which will also be discussed in the following sections. The ILES results are closer to the experiment than the hybrid RANS/LES.

B. Velocity Profiles

A quantitative comparison between the flowfield in the experiment, the results obtained with the present ILES approach

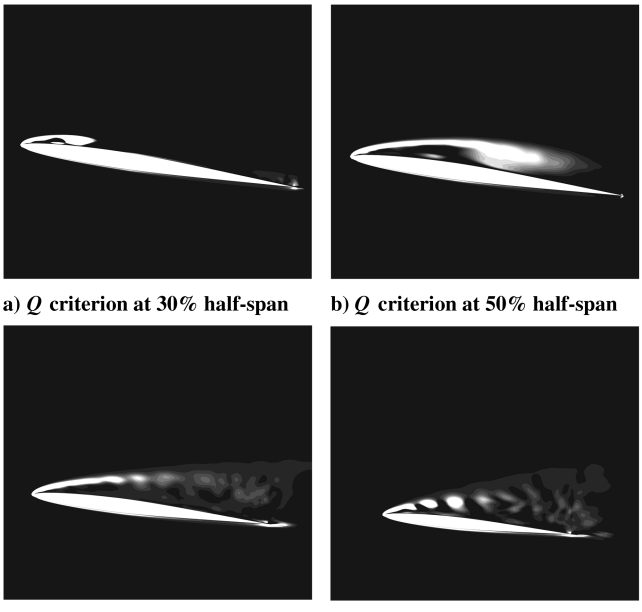

a) Q criterion at 30% half-span **b) Q criterion at 50% half-span**

c) Q criterion at 70% half-span **d) Q criterion at 90% half-span**

Fig. 5 Contours of the Q criterion obtained by the present simulation at different locations along the span of the wing.

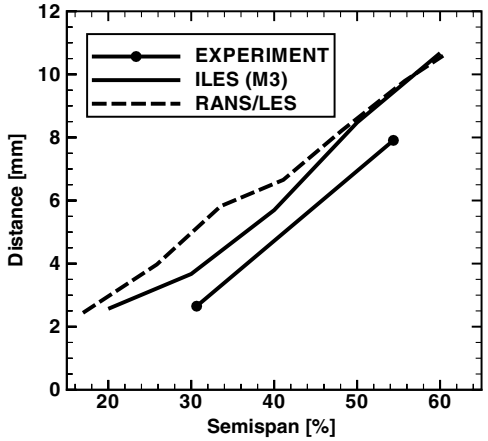

Fig. 6 Comparison of the clearance between the vortex core position and the wing surface as obtained in the experiment, with ILES and the hybrid RANS/LES.

using high-resolution methods, and the hybrid RANS/LES simulation [33] on a finer grid (approximately double the size of the grid used in ILES) comprising 23.6 million nodes has been performed. The time-averaged velocity and Reynolds stress profiles as a function of the distance from the wing have been calculated from the experimental data sets measured nearly normal to the surface at several positions along the half-span and the local chord by three-dimensional LDA. It should be noted that the velocities and corresponding Reynolds stresses presented here have not been decomposed into tangential and normal directions to the wall; thus, they represent the streamwise u), spanwise v, and azimuthal w components.

Figure 7 shows the time-averaged velocity components for different locations along the local chord at 30% half-span. Near the leading edge (Fig. 7a), all streamwise velocity profiles are in good agreement, with minor differences regarding the position and magnitude of the peak. The present simulation, however, deviates from the experiment and the hybrid RANS/LES near the surface at 10% local chord. This behavior is associated with the size and

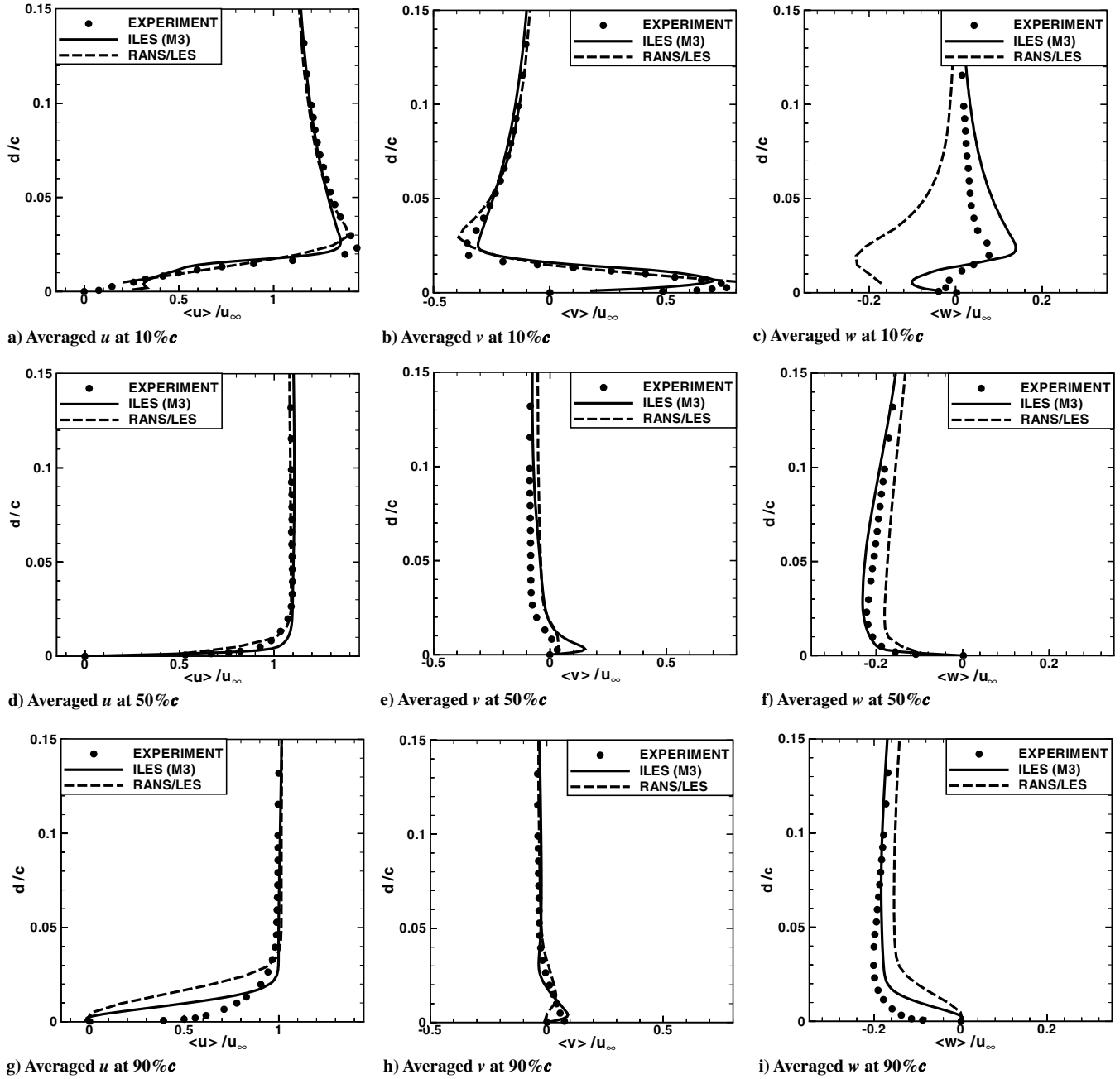

a) Averaged u at 10%c **b) Averaged v at 10%c** **c) Averaged w at 10%c**

d) Averaged u at 50%c **e) Averaged v at 50%c** **f) Averaged w at 50%c**

g) Averaged u at 90%c **h) Averaged v at 90%c** **i) Averaged w at 90%c**

Fig. 7 Comparison between averaged velocity profiles from the experiments, the results obtained with ILES and the hybrid RANS/LES for different locations along the local chord at 30% half-span.

strength of the secondary vortical region. The spanwise component in Fig. 7b features the characteristic crossflow profile observed in swept-wing aerodynamics. Close to the wing surface, the negative pressure gradient leads to an outflow toward the wing tip, whereas away from the surface, the fluid tries to fill the gap opened by the higher displacement near the wing root and thus inflow occurs. Here, the magnitude of both minimum and maximum velocity are slightly underpredicted by ILES, but overpredicted by the hybrid simulation. Regarding the azimuthal component (Fig. 7c), the general shape of the profile dictated by the existence of the secondary vorticity and the position of the free shear layer is well captured in the present ILES simulation. However, the near-wall vortical region could not be predicted by the hybrid RANS/LES approach at this location, and thus this simulation produces an entirely different result.

At 30% half-span and 50% local chord (Figs. 7d–7f), the profiles extracted from the experiment, the ILES, and the hybrid RANS/LES simulations exhibit a fairly similar shape for all three velocity components. The present simulation predicts a slightly thinner boundary layer and a stronger crossflow component near the surface than observed in the experiment and the hybrid RANS/LES. On the other hand, the hybrid approach overpredicts the magnitude of the azimuthal portion of the flow in Fig. 7f. It should be noted that this specific location is just upstream of the inboard separated zone. Hence, the influence of the detached flow on the velocity profiles here is only marginal. However, this situation does change when approaching the trailing edge, as shown in Figs. 7g–7i. Both simulations predict incipient flow separation at 90% local chord, which is reflected clearly in the profiles of the streamwise and the azimuthal velocity. As the experimental oil-film visualization does not suggest any detachment in this area, differences regarding the velocity profiles are expected. Yet, the crossflow component predicted by ILES is in much closer agreement to the experimental data than the hybrid RANS/LES.

The averaged velocity profiles for the midwing section at 50% half-span are presented in Fig. 8. The secondary vortical region has considerably developed when compared with the inboard position,

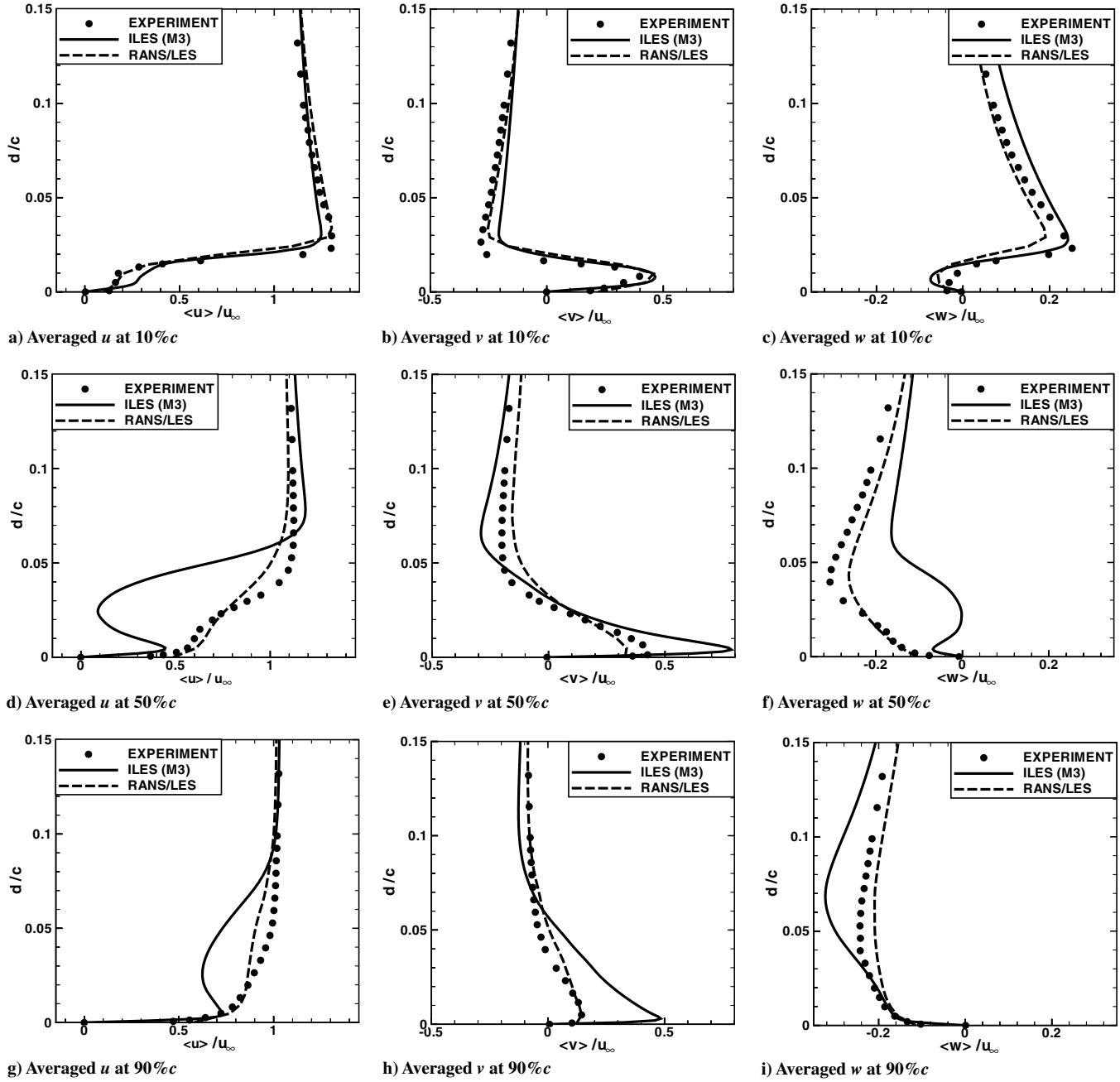

a) Averaged *u* at 10%*c* b) Averaged *v* at 10%*c* c) Averaged *w* at 10%*c*

d) Averaged *u* at 50%*c* e) Averaged *v* at 50%*c* f) Averaged *w* at 50%*c*

g) Averaged *u* at 90%*c* h) Averaged *v* at 90%*c* i) Averaged *w* at 90%*c*

Fig. 8 Comparison between averaged velocity profiles from the experiments, the results obtained with ILES and the hybrid RANS/LES for different locations along the local chord at 50% half-span.

and the effect on the streamwise velocity component at 10% local chord is clearly visible in the experiment as well as in both simulations (Fig. 8a). The $\langle u \rangle$ profiles near the leading edge compare well, with ILES predicting a small overshoot near the surface, indicating stronger vorticity. The hybrid RANS/LES yields a peak velocity further from the wing than the experiment and ILES. The spanwise and the azimuthal velocity in Figs. 8b and 8c obtained by both simulations are slightly overpredicted near the wall and tend to peak at a lower magnitude away from the wing with respect to the experiment.

The agreement is poor at the half-chord position in Fig. 8. The velocity profiles are strongly affected by the premature nonlinear growth of the leading-edge vortex observed in the present simulation, associated with an inadequate representation of the shear layer, which manifests itself in large discrepancies between the ILES prediction and the experiment. The streamwise and the azimuthal velocities are decelerated in the vicinity of the wing (Figs. 8d and 8f), and the cross-stream component is amplified by the rotation of the large vortex (Fig. 8e). The hybrid RANS/LES, on the other hand, is closer to the experimental data. However, the kink in the $\langle u \rangle$ profile measured in the experiment representing the influence of the leading-edge vortex is also not reproduced adequately by the hybrid approach, though the grid resolution is twice that of ILES. This suggests that the extent of the LEV in the streamwise direction is underpredicted in the hybrid RANS/LES. The same observations can be made for the location close to the trailing edge at 90% local chord, albeit the effect is diminished.

Further outboard, the experimental skin-friction lines have revealed a nonlinear spreading of the leading-edge vortex similar to the present simulation. In this region of enhanced interaction with the fully separated-flow regime toward the wing tip, the accuracy of the ILES prediction appears to recover (Fig. 9). Near the leading edge, at 10% local chord, the streamwise velocity is already reversed, and thus a thickening of the boundary can be observed in Fig. 9a. This effect is captured by ILES using high-resolution methods, whereas the hybrid RANS/LES approach fails. Consequently, both spanwise and azimuthal velocity profiles obtained by hybrid RANS/LES do not match the experimental data at this location, with all velocity

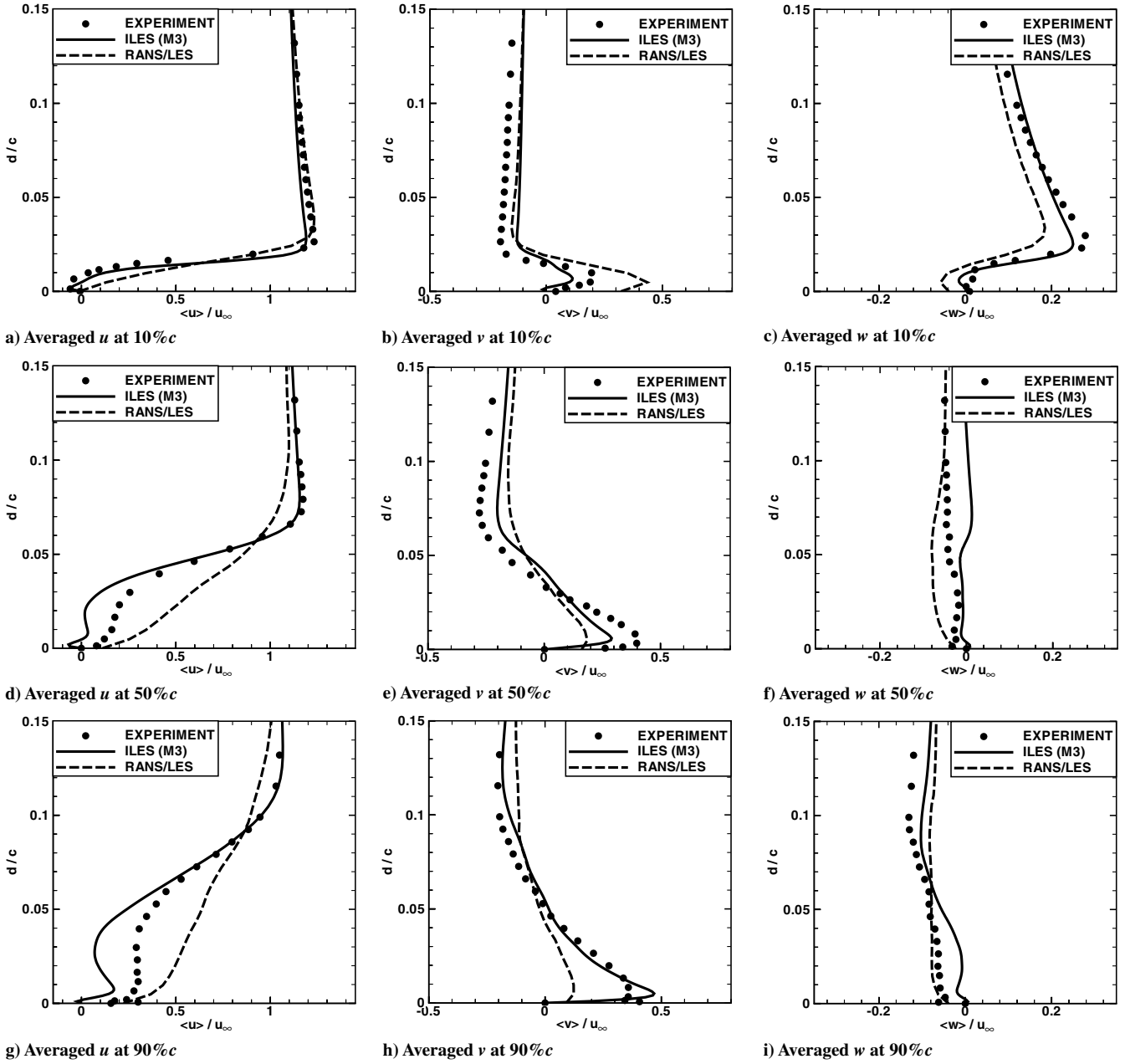

a) Averaged u at 10%c b) Averaged v at 10%c c) Averaged w at 10%c

d) Averaged u at 50%c e) Averaged v at 50%c f) Averaged w at 50%c

g) Averaged u at 90%c h) Averaged v at 90%c i) Averaged w at 90%c

Fig. 9 Comparison between averaged velocity profiles from the experiments, the results obtained with ILES and the hybrid RANS/LES for different locations along the local chord at 70% half-span.

components being more accurately predicted by ILES. Although the flow is not detached at positions closer to the trailing edge, it appears that the present results approach the experimental velocity profiles in Figs. 9d–9f, but predictions with the hybrid RANS/LES are still hindered by the erroneous flow development near the leading edge. Despite being somewhat underestimated in terms of magnitude, the spanwise (and, in particular, the streamwise) flow component at 50% local chord from the ILES simulation follows the shape of the experimental profile closely. Only weak azimuthal motion can be observed; hence, minor differences regarding the $\langle w \rangle$ velocity in Fig. 9f are deemed less important. At 90%s (Figs. 9g–9i), the profiles exhibit a similar behavior, except that the experimental spanwise velocity and the corresponding component obtained by ILES are in better agreement than at 50% local chord. Yet, this is not the case for $\langle w \rangle$ near the wing surface.

The observations discussed previously for the spanwise location at 70%s become more pronounced in the fully separated and turbulent region close to the wing tip at 90% half-span, as shown in Fig. 10. It should be noted that the improvements are partly due to the finer grid clustering in this area, but the flow is certainly still highly underresolved on the computational mesh used in ILES. On one hand, the profiles of all velocity components as predicted by ILES are nearly identical to the experimental data at most chordwise positions. Admittedly, small discrepancies regarding the inboard motion and the peak vertical velocity can be detected near the leading edge at 10%s (see Figs. 10b and 10c, respectively). On the other hand, the hybrid RANS/LES approach completely suppresses separation, probably because the RANS strategy applied here cannot treat the massive flow detachment adequately. Thus, the results obtained with the hybrid RANS/LES approach exhibit significant discrepancies with the experiment throughout the fully turbulent region.

C. Turbulence Energy Profiles

Figure 11 shows the turbulence energy profiles from the experiments, the results obtained with the present ILES, and hybrid

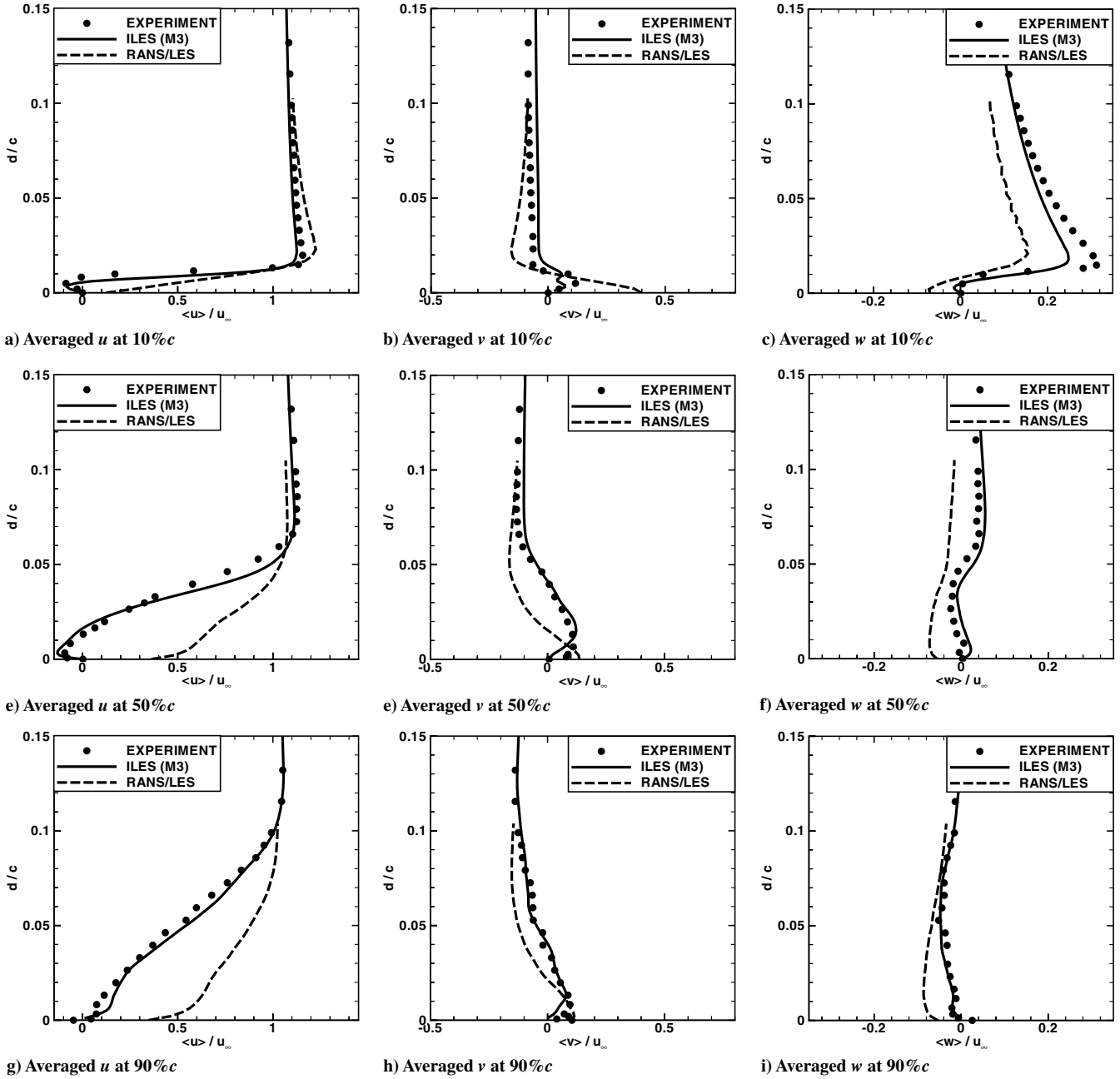

a) Averaged u at 10%c b) Averaged v at 10%c c) Averaged w at 10%c

e) Averaged u at 50%c e) Averaged v at 50%c f) Averaged w at 50%c

g) Averaged u at 90%c h) Averaged v at 90%c i) Averaged w at 90%c

Fig. 10 Comparison between averaged velocity profiles from the experiments, the results obtained with ILES and the hybrid RANS/LES for different locations along the local chord at 90% half-span.

RANS/LES for different locations along the local chord at 30 and 50% half-span. It can be noticed that the flow is essentially laminar at the inboard section (i.e., 30%s) over most of the chord length (Figs. 11c and 11e). Only the shear layer emanating from the leading edge produces a significant level of turbulence, as observed in the experiment and in the hybrid RANS/LES simulation at 10% local chord (Fig. 11a). Here, the hybrid RANS/LES overestimates the peak by about 40%, whereas ILES underpredicts the peak energy, because the relatively thin layer cannot be represented adequately on the given grid with only six cells across the shear layer. This is related to the specific grid requirements of the spatial discretization scheme employed here, as discussed in Sec. III. In a case of severely underresolved flow, it is expected that the fluctuating energy levels are lower when compared with the experimental data. If the flow is adequately resolved, however, a numerical solution should never overestimate the turbulence kinetic energy, which raises questions about the results obtained by the hybrid RANS/LES approach at this location. Furthermore, a second peak associated with the secondary vortical region can be detected closer to the wing surface in the profile predicted by the ILES approach that, in line with the previous observations, does not appear in the experiment.

At the midspan position 50%s, shown in Figs. 11b–11f, a similar scenario is presented near the leading edge. The turbulence level in the ILES simulation is still too low when compared with the experiment. However, the effect of the secondary vortical region is now clearly visible in all three profiles in Fig. 11b. A less favorable impression is left by the hybrid RANS/LES at this location. It seems that the existence of the secondary vortical zone influences the shear layer and alters its character; hence, the peak energy is suddenly underestimated by a factor of approximately 5, which is not consistent with the prediction of the shear layer at other locations near the leading edge. As can be seen at the midchord position (Fig. 11d), the behavior of the free shear layer has serious consequences for the downstream development of the flow. In the present ILES, the onset of LEV roll-up can be detected just after 50%c ,and thus the shear layer is still intact at this location, which is

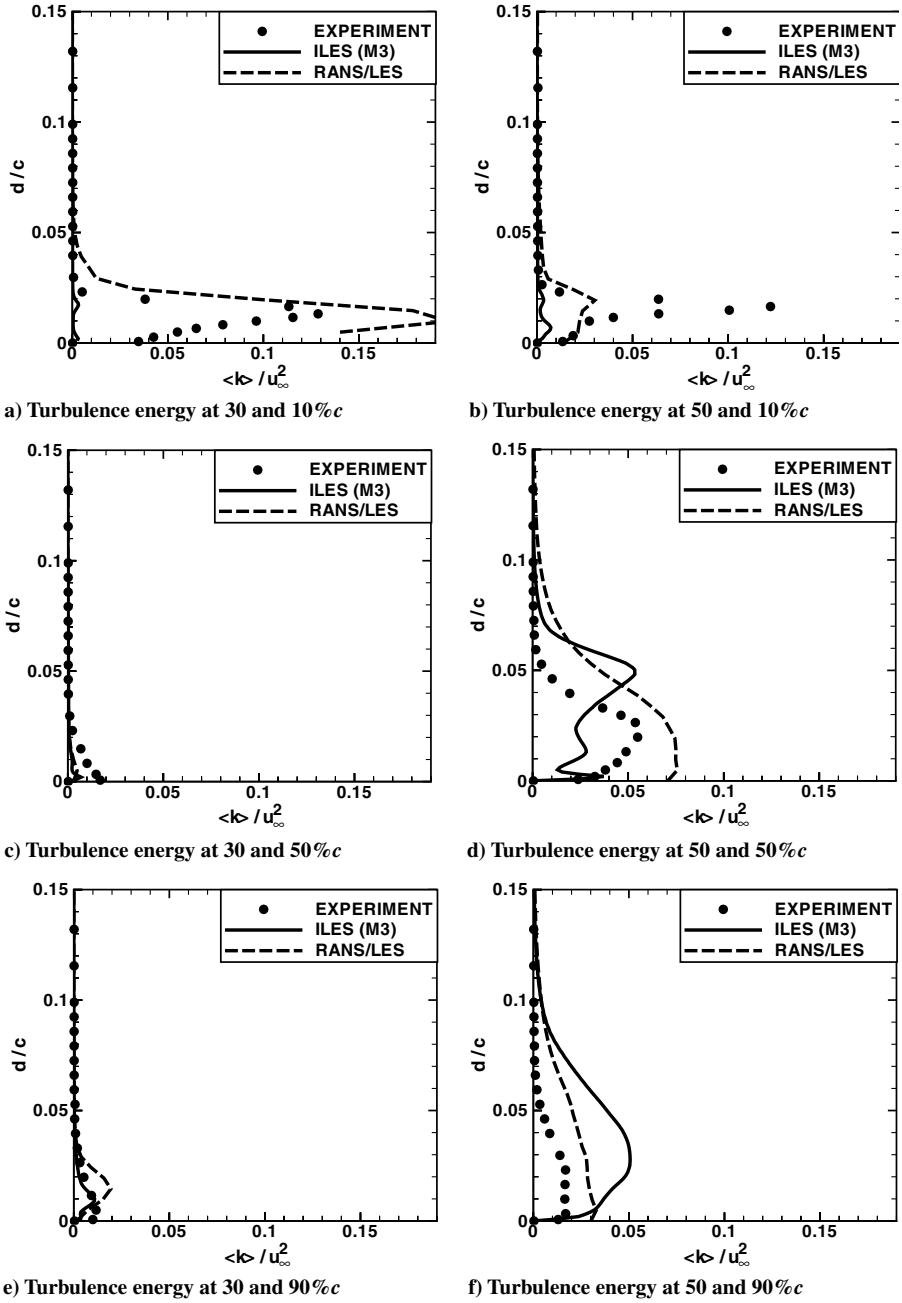

a) Turbulence energy at 30 and 10%c

b) Turbulence energy at 50 and 10%c

c) Turbulence energy at 30 and 50%c

d) Turbulence energy at 50 and 50%c

e) Turbulence energy at 30 and 90%c

f) Turbulence energy at 50 and 90%c

Fig. 11 Comparison between averaged turbulence energy profiles from the experiments, the results obtained with ILES and the hybrid RANS/LES for different locations along the local chord at 30 and 50% half-span.

reflected in the peak turbulence energy away from the wing. A result of the delayed leading-edge vortex formation is the increased growth rate due to the diminishing influence of the wall, thereby leading to a seemingly premature nonlinear spreading of the vortex. Two additional peaks, albeit smaller, can be observed in the profile from the ILES simulation. Close to the solid surface, the strong crossflow component, caused by the large extent of the leading-edge vortex, also yields an increase in turbulence energy. Furthermore, the influence of the LEV can be felt between the wing and the shear layer, as implied by the second peak in Fig. 11d. Both profiles obtained with the experiment and the hybrid RANS/LES suggest the presence of a developed leading-edge vortex at 50%c with the level of turbulence decreasing toward the trailing edge. Here, at 90%c, the full profile predicted by ILES indicates a stronger influence of the LEV when compared with the experiment and the hybrid RANS/LES (Fig. 11f).

Consistent with the aforementioned comments on grid resolution in the shear layer, a slightly thicker shear layer leads to stronger velocity fluctuations, as observed in the present simulation near the leading edge for the 70% half-span section (Fig. 12a). However, the peak turbulence energy is still underpredicted by the ILES approach, and the clearance between wing surface and the shear layer appears too low. The reversed flow situation close to the leading edge is not captured by the hybrid RANS/LES, and the profile obtained by the hybrid RANS/LES does not start from zero at the wall, which is clearly an *unphysical* result. At the 70% half-span station, the main vortex core has turned toward the trailing edge and undergone a breakup mechanism. Therefore, the shear layer does not roll up. In fact, it still affects the turbulence energy profiles at 50% local chord, as indicated by the peaks in both the experiment and ILES (Fig. 12c), but not in the hybrid RANS/LES results. However, the present simulation overpredicts the crossflow fluctuations near the wing surface already observed at the half-chord position for 50%s. Close to the trailing edge, the level of turbulence diminishes for the hybrid RANS/LES, whereas it increases in the ILES simulation due to enhanced mixing caused by the large vortex.

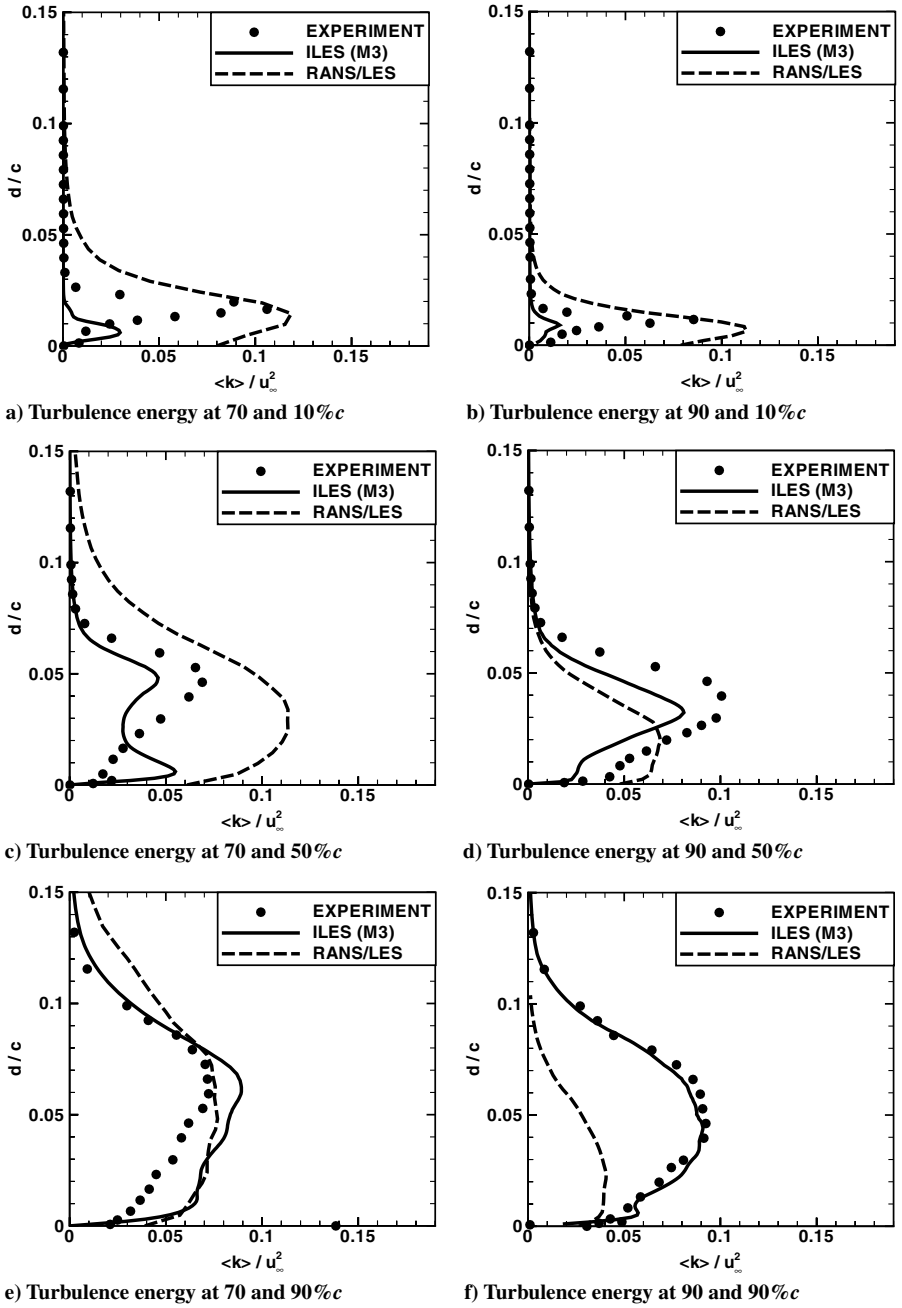

a) Turbulence energy at 70 and 10%c

b) Turbulence energy at 90 and 10%c

c) Turbulence energy at 70 and 50%c

d) Turbulence energy at 90 and 50%c

e) Turbulence energy at 70 and 90%c

f) Turbulence energy at 90 and 90%c

Fig. 12 Comparison between averaged turbulence energy profiles from the experiments, the results obtained with ILES and the hybrid RANS/LES for different locations along the local chord at 70 and 90% half-span.

The results for 90%s (Figs. 12b–12f) exhibit a similar behavior to those at 70% half-span. Here, the position of the free shear layer emanating from the leading edge is in better agreement with the experiment than at the inboard station, but the peak magnitude is underestimated again. Moreover, the turbulence energy profiles obtained by the present ILES using high-resolution methods closely match the shape of the experimental results further downstream and are virtually identical in the vicinity of the trailing edge. As anticipated, however, the hybrid RANS/LES approach fails to predict the flow in this fully turbulent region dominated by massive separation.

V. Conclusions

The implicit large-eddy simulation approach using high-resolution methods has been applied to the flow around a swept-wing geometry of practical aeronautical interest. This highly complex problem combines large-scale separation with substantial regions of attached flow in which the realistic representation of near-wall effects are of paramount importance.

It has been found that both simulation approaches predict an area of mildly reversed flow near the wing root and leading-edge vortex breakdown beyond approximately 50% half-span, whereas the experiment suggests that an inboard dead-air region and vortex breakdown cannot be clearly identified. The large-scale flow features are reasonably well represented by the two numerical approaches. The hybrid RANS/LES fails completely in the fully turbulent and separated regions, as well as closer to the wing tip. This indicates that the simplified RANS-type treatment of the near-wall region neglecting advective and pressure terms cannot be applied in this case. Although ILES has been carried out on a grid of half the size, it was found to be significantly more accurate than hybrid RANS/LES in these regions. However, the grid resolution in the free shear layer emanating from the leading edge of the wing needs to be increased for the ILES simulation to give a better representation of the fluctuating energy levels. Additionally, the hybrid approach appears to be more accurate in the attached-flow regions.

It should be highlighted that the computational grids employed in the two simulations differ substantially. For the hybrid approach, 23.6 million nodes have been distributed using a H-H-type topology of similar extent to the C-O-type mesh used in ILES, which, however, has only half the number of nodes. Furthermore, the two grids are distinguished by the specific requirements in the vicinity of the wing surface. In ILES, the z^+ ranges from 1 to 5, whereas the hybrid RANS/LES grid yields values between 20 and 40. Because of the significant grid clustering in ILES, the grid resolution in the free shear layer is fairly coarse. This has a severe impact on the calculations regarding the development of the leading-edge vortex as exemplified for the section at 50% half-span. However, when the LEV is not present and the flow is fully turbulent (i.e., closer to the wing tip), the influence of the shear layer is diminished and the ILES results are in very good agreement with the experiment. In general, this investigation has demonstrated that high-resolution methods can be applied to complex separated flows without any modification and without resorting to turbulence models.

Acknowledgments

The authors would like to acknowledge financial support from the Engineering and Physical Sciences Research Council (EPSRC) (GR/S27436/01) through the MSTTAR Defence Aerospace Research Partnership (DARP), supported by EPSRC, the Ministry of Defence, Department of Trade and Industry, BAE Systems, Rolls-Royce, and QinetiQ. They would also like to acknowledge stimulating discussions with Ning Li and Michael Leschziner at Imperial College and Shanying Zhang and John Turner at the University of Manchester. The experimental results have been provided by the University of Manchester.

References

[1] Cummings, R. M., Forsythe, J. R., Morton, S. A., and Squires, K. D., "Computational Challenges in High Angle of Attack Flow Prediction," *Progress in Aerospace Sciences*, Vol. 39, No. 5, 2003, pp. 369–384. doi:10.1016/S0376-0421(03)00041-1

[2] Gordnier, R. E., "Numerical Simulation of a 65-Degree Delta Wing Flowfield," *Journal of Aircraft*, Vol. 34, No. 4, July–Aug. 1997, pp. 492–499. doi:10.2514/2.2218

[3] Gordnier, R. E. and Visbal, M. R., "Compact Difference Scheme Applied to Simulation of Low-Sweep Delta Wing Flow," *AIAA Journal*, Vol. 43, No. 8, Aug. 2005, pp. 1744–1752. doi:10.2514/1.5403

[4] Gordnier, R. E., and Visbal, M. R., "High-Order Simulation of Low Sweep Delta Wing Flows Using ILES and Hybrid RANS/ILES Models," AIAA Paper 2006-0504, Jan. 2006.

[5] Rizzetta, D. P., "Numerical Simulation of the Interaction Between a Leading-Edge Vortex and a Vertical Tail," AIAA Paper 1996-2012, June 1996.

[6] Brandsma, F. J., Kok, J. C., Doi, H. S., and Elsenaar, A., "Leading Edge Vortex Flow Computations and Comparison with DNW-HST Wind Tunnel Data," NLR, National Aerospace Lab., Rept. NLR-TP-2001-238, Amsterdam, 2001.

[7] Mellen, C. P., Fröhlich, J., and Rodi, W., "Lessons from the European LESFOIL Project on LES of Flow Around an Airfoil," AIAA Paper 2002-0111, Jan. 2002.

[8] Morgan, P. E. and Visbal, M. R., "Large-Eddy Simulation Modeling Issues for Flow Around Wing Sections," AIAA Paper 2003-4152, June 2003.

[9] Mary, I., and Sagaut, P., "Large Eddy Simulation of Flow Around an Airfoil Near Stall," *AIAA Journal*, Vol. 40, No. 6, June 2002, pp. 1139–1145. doi:10.2514/2.1763

[10] Dahlström, S., and Davidson, L., "Large Eddy Simulation Applied to a High-Reynolds Flow Around an Airfoil Close to Stall," AIAA Paper 2003-0776, Jan. 2003.

[11] Shan, H., Jiang, L., and Liu, C., "Direct Numerical Simulation of Flow Separation Around a NACA 0012 Airfoil," *Computers and Fluids*, Vol. 34, No. 9, 2005, pp. 1096–1114. doi:10.1016/j.compfluid.2004.09.003

[12] Drikakis, D., and Rider, W. J., *High-Resolution Methods for Incompressible and Low-Speed Flows*, Springer, New York, 2004.doi: 10.1016/S0376-0421(03)00075-7

[13] Drikakis, D., "Advances in Turbulent Flow Computations Using High-Resolution Methods," *Progress in Aerospace Sciences*, Vol. 39, Nos. 6–7, 2003, pp. 405–424. doi:10.1016/S0376-0421(03)00075-7

[14] Fureby, C., and Grinstein, F. F., "Large Eddy Simulation of High Reynolds Number Free and Wall Bounded Flows," *Journal of Computational Physics*, Vol. 181, No. 1, 2002, pp. 68–97. doi:10.1006/jcph.2002.7119

[15] Grinstein, F. F., and Fureby, C., "Recent Progress on MILES for High Reynolds Number Flows," *Journal of Fluids Engineering*, Vol. 124, Dec. 2002, pp. 848–861. doi:10.1115/1.1516576

[16] Fureby, C., "ILES and LES of Complex Engineering Turbulent Flows," *Journal of Fluids Engineering*, Vol. 129, No. 12, Dec. 2007, pp. 1514–1523. doi:10.1115/1.2801370

[17] Fureby, C., and Grinstein, F. F., "Monotonically Integrated Large Eddy Simulation of Free Shear Flows," *AIAA Journal*, Vol. 37, No. 5, May 1999, pp. 544–556. doi:10.2514/2.772

[18] Margolin, L. G., and Rider, W. J., "A Rationale for Implicit Turbulence Modeling," *International Journal for Numerical Methods in Fluids*, Vol. 39, No. 9, 2002, pp. 821–841. doi:10.1002/fld.331

[19] Grinstein, F. F., Margolin, L. G., and Rider,W. J. (ed.), *Implicit Large Eddy Simulation*, Cambridge Univ. Press, Cambridge, England, U.K., 2007.

[20] Eberle, A., "Characteristic Flux Averaging Approach to the Solution of Euler's Equations," *Computational Fluid Dynamics*, VKI Lecture Series, von Karman Inst. of Fluid Dynamics, Rhode-St.-Genèse, Belgium, 1987.

[21] Drikakis, D., *Godunov Methods: Theory and Applications*, Kluwer Academic, Norwell, MA, 2001, pp. 263–283.

[22] Drikakis, D., Govatsos, P. A., and Papatonis, D. E., "A Characteristic-Based Method for Incompressible Flows," *International Journal for Numerical Methods in Fluids*, Vol. 19, No. 8, 1994, pp. 667–685. doi:10.1002/fld.1650190803

[23] Harten, A., "High Resolution Schemes for Hyperbolic Conservation," *Journal of Computational Physics*, Vol. 49, No. 3, 1983, pp. 357–393. doi:10.1016/0021-9991(83)90136-5

[24] Zóltak, J., and Drikakis, D., "Hybrid Upwind Methods for the Simulation of Unsteady Shock-Wave Diffraction over a Cylinder," *Computer Methods in Applied Mechanics and Engineering*, Vol. 162, Nos. 1–4, 1998, pp. 165–185. doi:10.1016/S0045-7825(97)00342-3

[25] Toro, E. F., *Riemann Solvers and Numerical Methods for Fluid Dynamics—A Practical Introduction*, Springer–Verlag, Heidelberg, Germany, 1997.

[26] Spiteri, R. J., and Ruuth, S. J., "A New Class of Optimal High-Order Strong-Stability-Preserving Time Discretization Methods," *SIAM Journal on Numerical Analysis*, Vol. 40, No. 2, 2002, pp. 469–491. doi:10.1137/S0036142901389025

[27] Pope, S. B., *Turbulent Flows*, Cambridge Univ. Press, Cambridge, England, U.K., 2000.

[28] Thornber, B., Mosedale, A., and Drikakis, D., "On the Implicit Large Eddy Simulations of Homogeneous Decaying Turbulence," *Journal of Computational Physics*, Vol. 226, No. 2, 2007, pp. 1902–1929. doi:10.1016/j.jcp.2007.06.030

[29] Li, N., and Leschziner, M. A., "Large-Eddy Simulation of Flow over a Swept Wing with Approximate Near Wall Modeling," AIAA Paper 2007-1118, Jan. 2007.

[30] Temmerman, L., Hadžiabdić, M., Leschziner, M. A., and Hanjelić, K., "A Hybrid Two-Layer URANS/LES Approach for Large Eddy Simulation at High Reynolds Numbers," *International Journal of Heat and Fluid Flow*, Vol. 26, No. 2, 2005, pp. 173–190. doi:10.1016/j.ijheatfluidflow.2004.07.006

[31] Tessicini, F., Temmerman, L., and Leschziner, M. A., "Approximate Near Wall Treatments Based on Zonal and Hybrid RANS-LES Methods for LES at High Reynolds Numbers," *International Journal of Heat and Fluid Flow*, Vol. 27, No. 5, 2006, pp. 789–799. doi:10.1016/j.ijheatfluidflow.2006.03.024

[32] Tessicini, F., Li, N., and Leschziner, M. A., "Large-Eddy Simulation of Three-Dimensional Flow Around a Hill-Shaped Obstruction with a Zonal Near Wall Approximation," *International Journal of Heat and Fluid Flow*, Vol. 28, No. 5, 2007, pp. 894–908. doi:10.1016/j.ijheatfluidflow.2007.01.006

[33] Li, N., and Leschziner, M. A., "Large-Eddy Simulation of Separated Flow over a Swept Wing with Approximate Near Wall Modelling," *The Aeronautical Journal*, Vol. 111, No. 1125, Nov. 2007, pp. 689–697.

[34] Jeong, J., and Hussain, F., "On the Identification of a Vortex," *Journal of Fluid Mechanics*, Vol. 285, No. 1, 1995, pp. 69–94. doi:10.1017/S0022112095000462

P. Givi
Associate Editor